

IMECE2008-67844

## MEMS PRESSURE SENSOR ARRAY FOR AEROACOUSTIC ANALYSIS OF THE TURBULENT BOUNDARY LAYER

Joshua S. Krause  
Robert D. White \*

Department of Mechanical Engineering  
Tufts University  
Medford, Massachusetts 02155  
Email: r.white@tufts.edu

Mark J. Moeller  
Judith M. Gallman

Spirit AeroSystems, Inc.  
Wichita, Kansas 67278-0008

Rich De Jong

Department of Mechanical Engineering  
Calvin College  
Grand Rapids, Michigan 49546-4403

### ABSTRACT

*The design, fabrication, and characterization of a surface micromachined, front-vented, 64 channel (8×8), capacitively sensed pressure sensor array is described. The array was fabricated using the MEMSCAP PolyMUMPs® process, a three layer polysilicon surface micromachining process. An acoustic lumped element circuit model was used to design the system. The results of our computations for the design, including mechanical components, environmental loading, fluid damping, and other acoustic elements are detailed. Theory predicts single element sensitivity of 1 mV/Pa at the gain stage output in the 400-40,000 Hz band. A laser Doppler velocimetry (LDV) system has been used to map the spatial motion of the elements in response to electrostatic excitation. A strong resonance appears at 480 kHz for electrostatic excitation, in good agreement with mathematical models. Static stiffness measured electrostatically using an interferometer is 0.1 nm/V<sup>2</sup>, similar to the expected stiffness. Preliminary acoustic sensitivity studies show single element acoustic sensitivity (as a function of frequency) increasing from 0.01 mV/Pa at 200 Hz to 0.16 mV/Pa at 2 kHz. A more in depth analysis of acoustic sensitivity is ongoing.*

### NOMENCLATURE

$a$  Radius of diaphragm  
 $a_{eff}$  Effective radius of diaphragm  
 $t_{dia}$  Thickness of diaphragm

$a_{gap}$  Radius of the gap cavity  
 $t_{gap}$  Thickness of air gap  
 $V_{gap}$  Volume of air gap  
 $n$  Number of holes in the diaphragm  
 $a_{hole}$  Radius of diaphragm vent holes  
 $C_c$  Center-to-center spacing of vent holes  
 $\rho$  Density of air  
 $c$  Speed of sound  
 $\mu$  Viscosity of air  
 $\rho_{dia}$  Density of diaphragm (Polysilicon)  
 $E$  Modulus of elasticity of diaphragm  
 $\nu$  Poisson's ratio of diaphragm  
 $V_{bias}$  Bias voltage applied  
 $\epsilon_0$  Permittivity of free space  
 $C_{fb}$  Feedback capacitor in charge amplifier  
 $R_{fb}$  Feedback resistor in charge amplifier  
 $R_{stray}$  Stray resistance between diaphragm and metal trace  
 $C_{block}$  DC blocking capacitor  
 $R_{block}$  Resistor to ground after DC blocking capacitor  
 $f_b$  Break frequency for AD621  
 $R_{A1}$  Lumped element resistance 1 due to air  
 $R_{A2}$  Lumped element resistance 2 due to air  
 $M_{A1}$  Lumped element mass loading due to air  
 $C_{A1}$  Lumped element compliance due to air  
 $C_{cav}$  Lumped element compliance of the cavity  
 $C_{dia}$  Lumped element compliance of the diaphragm  
 $M_{dia}$  Lumped element mass of diaphragm

\*Address all correspondence to this author.

$R_{through}$  Lumped element resistance through holes in the diaphragm  
 $S$  Škvor's formula  
 $C_f$  Correction factor to Škvor's formula  
 $R_{squeeze}$  Lumped Element resistance due to squeeze film damping  
 $R_{hole}$  Lumped Element resistance of the holes in the diaphragm  
 $N$  Transducer coupling parameter  
 $U_{dia}$  Volume velocity of diaphragm  
 $I$  Current  
 $V_{ac}$  AC voltage  
 $P_{Elect}$  Electrostatic pressure

## INTRODUCTION

Turbulence has been plaguing transport aircraft designers for over fifty years. Tennekes and Lumley pose seven qualities that characterize turbulence. They present turbulence as being irregular, diffuse, and often associated with large Reynolds numbers. It is a three-dimensional vortical fluctuation following a continuum model and dissipates over time [1]. Several models have been analytically and experimentally obtained to understand the complex nature of turbulence, but as a result of the stochastic nature, a theoretical model is more difficult to obtain. Therefore, using hot wire anemometry, shear stress sensors, and pressure sensors at the microscopic level will help to obtain empirical results describing the phenomena associated with turbulence and more importantly the turbulent boundary layer (TBL).

The sources of structural excitation and radiative noise in passenger aircrafts are noise due to the interior environment, the engine, and the fluctuations in wall pressure beneath the TBL. The noise generated by the TBL is considered the most dominant noise source on transport aircrafts [2]. In order to model the structural response of an aircraft, spectral levels at both low and high wavenumbers are needed [3]. The low wavenumber assessment is vital due to the fact that structural resonances take place at low wavenumbers and acoustic noise is generally emitted at low wavenumbers compared to convective turbulent energy [4]. Although low wavenumbers are important for the analysis of acoustic noise generation and structural vibrations, the high convective wavenumbers are where the greatest energy levels are present in the turbulent field, and hence need to be understood. A lack of empirical knowledge as a result of the limits due to conventional instrumentation is one reason for our poor understanding of turbulence [5]. MEMS pressure sensors may alleviate this issue due to their small size and the ability to fabricate multiple microphones in an array. The challenge in MEMS arrays is achieving good matching between elements in the array and across arrays. In addition, due to their small size, the microphones necessarily have low sensitivity.

MEMS pressure sensors have been explored by many researchers over the past 25 years and many review articles can be

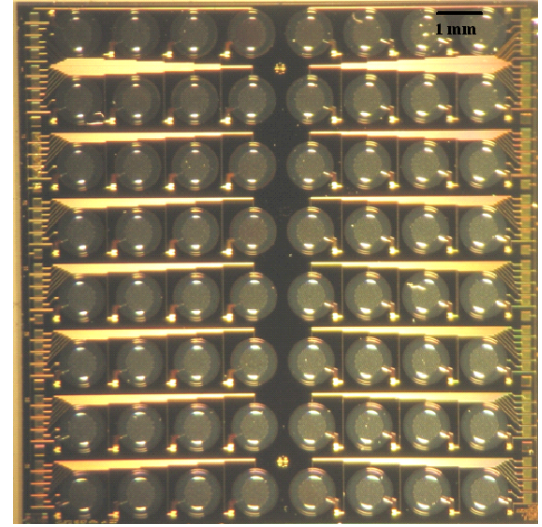


Figure 1. Photograph of the 64 microphones arrayed in an  $8 \times 8$  pattern.

found on them [6, 7, 8]. Most pressure sensors are developed for auditory applications, biomedical ultrasound arrays, and underwater applications [7]. Few microphones have been developed for aeroacoustic applications, possibly due to the difficulty of surviving the harsh environment. The Interdisciplinary Microsystems Group at the University of Florida Gainesville has done a great deal of work in this area and Martin *et al.* demonstrate a good summary of the previous microphones for aeroacoustic measurement [9].

## FABRICATION

The fabrication process of the 64 channel capacitive microphone array utilizes the MEMSCAP PolyMUMPs® process along with facilities at Tufts University. The polyMUMPs process is a foundry process that creates polysilicon structures via surface micromachining with a minimum feature size of  $2 \mu\text{m}$ . The process consists of seven physical layers, including 3 structural, 2 sacrificial and one metal layer. A photograph of a completed microphone sensor array is shown in Figure 3.

The fabrication process for a single element in the array is described. The process starts with a heavily phosphorus doped 150 mm n-type silicon wafer with a  $\langle 100 \rangle$  crystalline structure and resistivity of 1–2 ohm-cm. The process then uses low pressure chemical vapor deposition (LPCVD) to deposit a 600 nm layer of silicon nitride to isolate the electrical properties of the bulk silicon from the MEMS device. After the silicon is electrically isolated, the building of the structures is started by using the Poly 0 layer. The Poly 0 layer is a 500 nm layer of polysilicon that is also deposited by LPCVD, then patterned by photolithography to get the desired structure. After the first structural layer

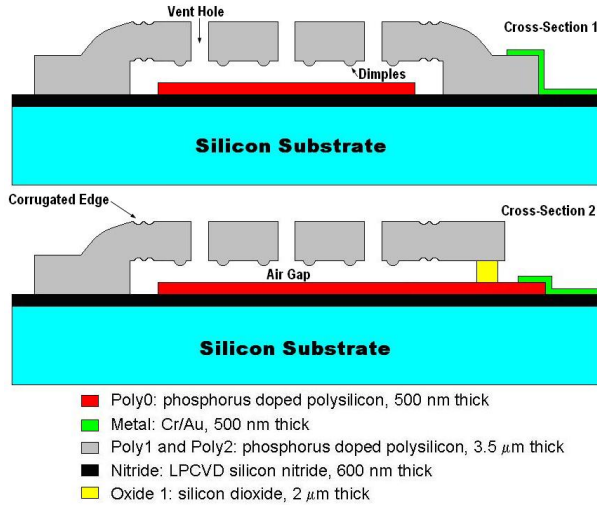


Figure 2. Schematic of one element in the microphone array showing two cross-sectional view. Cross-section 2 is through a region where the poly0 layer "tunnels" below the diaphragm to allow electrical connection to the bottom electrode. Cross-section 1 is through a more common region where there is no tunnel.

is deposited, a 2  $\mu\text{m}$  sacrificial layer is deposited by LPCVD and annealed for 1 hour at 1050° C. This structure is removed once the entire MUMPS process has been completed. However, before the release of the structure, several layers are patterned.

After the initial deposition of the PSG (1<sup>st</sup> Oxide) layer, a dimples mask is patterned by photolithography and etched out of the oxide using reactive ion etching (RIE). The depth of this etch is 750 nm. Next, the Anchor 1 mask will be patterned allowing the diaphragm to anchor to the nitride layer. The second structural (Poly 1) layer is then deposited to a thickness of 2  $\mu\text{m}$ . A 200 nm PSG layer is then deposited for 1 hour at 1050° C to dope the polysilicon with phosphorus while also reducing the stress in the deposition. The Poly 1 layer is then patterned with a hard mask which allows for a higher yield when the pattern is transferred to the polysilicon.

After the Poly 1 layer, a second sacrificial (2<sup>nd</sup> Oxide) layer is deposited and annealed at a thickness of 750 nm. This layer is patterned with a Poly1\_Poly2\_Via mask as well as an Anchor 2 mask. The Poly1\_Poly2\_Via layer provides etch holes to be patterned through the second oxide and the Anchor 2 mask is used to etch both the first and second oxides in one step. Following this, the final structural layer of polysilicon (Poly 2) is deposited to a 1.5  $\mu\text{m}$  thickness and then patterned. The same PSG process is applied to the Poly 2 layer to dope the layer in phosphorus. The final deposition layer is the metal layer. The metal layer is a 0.5  $\mu\text{m}$  layer of gold that provides an electrical connection for wiring and bonding.

Applying this process to the microphone array utilizes all

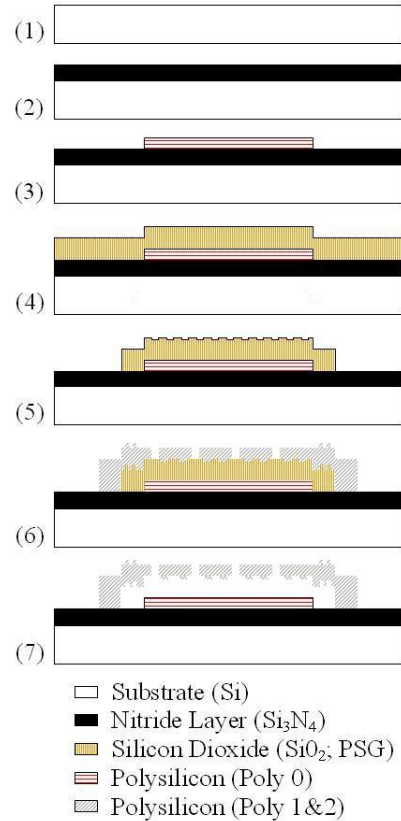


Figure 3. Schematic illustrating the fabrication process using the MEM-SCAP PolyMUMPS® process. (1) Bare silicon substrate. (2) Silicon Nitride layer is deposited as electrical isolation layer. (3) Bottom electrode is applied through Poly 0 layer. (4) Sacrificial oxide layer is deposited to create the cavity. (5) Dimples are patterned into 1<sup>st</sup> Oxide layer. (6) Poly 1 and Poly 2 layers are deposited as diaphragm. (7) Oxide is removed through HF release and sensor fabrication is complete.

layers in the process. The design for each sensor consisted of the base silicon wafer, followed by the nitride layer. The first structural layer to compose the actual sensor element is the Poly 0 layer. The Poly 0 layer is a circle with a radius of 290  $\mu\text{m}$  which acts as the bottom electrode for the microphone. Poly 0 is also used to "tunnel" under the diaphragm supports (using an oxide as insulation) to create the electrical connection between the bottom electrode and the wire which leads to the common biasing pads.

After the 1<sup>st</sup> Oxide layer is placed over Poly 0 layer, the Dimple layer is used to etch part of the way through the oxide 1 layer. This is used to put in place "dimples" on the bottom of the Poly 1 layer which will minimize the adhesion problems associated with stiction during the release of the structure at the end of the fabrication process. Through the use of the peel number

and assuming our structure acts like a doubly supported beam, we determined the dimples associated with reducing stiction will be spaced  $30\text{ }\mu\text{m}$  apart for a total of 201 dimples over the Poly 1 region [10]. Besides preventing adhesion, the dimple mask is used to create a corrugation of two concentric five micron wide circles. This corrugation allows for the partial relaxation of any residual stresses produced in the diaphragm during the fabrication process or during operation. This allows for an increase in sensitivity due to the reduction of the stress [11].

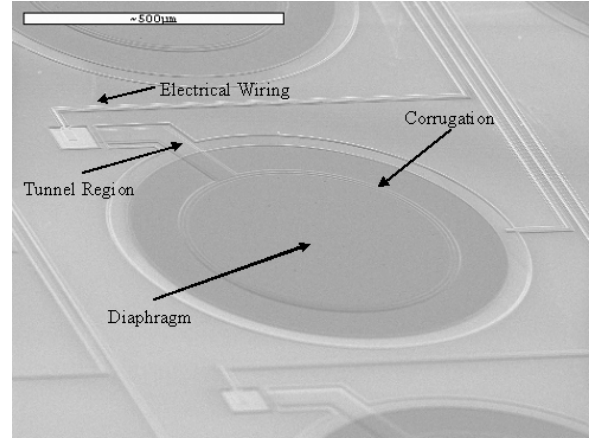
The first sacrificial layer (1<sup>st</sup> Oxide,  $2\text{ }\mu\text{m}$  thick) is then patterned using the Anchor 1 mask. This is drawn 20 microns around the Poly 0 layer in a torus shape. The Anchor 1 layer defines the inner dimension of the diaphragm, giving the mechanical diaphragm an inner radius of  $300\text{ }\mu\text{m}$ . Anchor 1 is also used to anchor the polysilicon/metal signal wires, guard bands, pads, and ground connections. Following the Anchor 1 layer, the Poly 1 layer is patterned. The Poly 1 layer is used both as the first part ( $2\text{ }\mu\text{m}$  of the total  $3.5\text{ }\mu\text{m}$ ) of the mechanical diaphragm and as part of the poly/metal wires. The Poly 1 portion of the diaphragm has a radius of  $455\text{ }\mu\text{m}$ , extending well into the Anchor region.

The next layer fabricated in the process is the Poly1.Poly2.Via layer which opens holes from the Poly1 to Poly2 layers. Due to the constraints of the bulk processing in the MUMPS process, we needed to combine the two layers (Poly1 and Poly2) to create a structure with a  $3.5\text{ }\mu\text{m}$  thickness. The Poly1.Poly2.Via layer is used for this purpose; it removes the interlayer dielectric (oxide 2) so that Poly 1 and Poly 2 are directly in contact, effectively forming a single  $3.5\text{ }\mu\text{m}$  thick polysilicon structural layer. The Anchor 2 layer opens holes for poly 2 directly to the Nitride or Poly0 layer. In this application the Anchor 2 is solely used to ground the elements to the substrate.

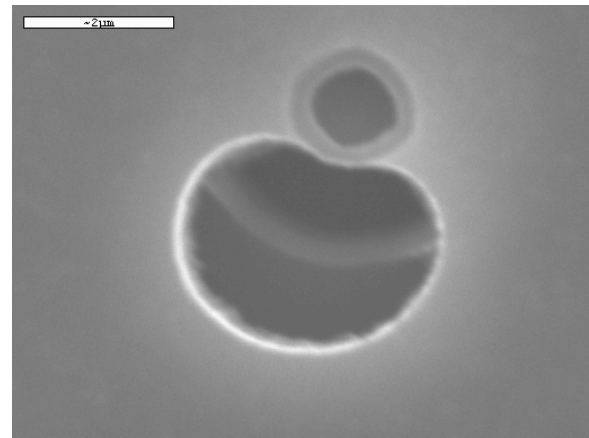
Holes are etched through both the poly 1 and poly 2 layers using the “hole 1” and “hole 2” layers. The hole through poly 1 is  $6\text{ }\mu\text{m}$  in diameter; the hole through poly 2 is  $4\text{ }\mu\text{m}$  in diameter. The holes have two purposes: (1) they will be used to introduce HF etchant during release to etch out the oxide 1 sacrificial layer (2) they act as frontside “vents” during operation, equalizing ambient pressure with gap pressure and providing damping.

Finally the Metal layer is used as a routing layer and as electrical pads around the outside of the device. All the wires and pads are combinations of polysilicon and metal, anchored directly to the nitride layer or to the bulk silicon, as appropriate. The final design implemented guard bands to ensure electrical connections, alignment markers and extra ground connections were applied to ensure a safe dissipation of static discharges, EMI and RFI signals. A uniform process was applied to the wiring of each element with guard bands located in between each wire (where each guard band connects to a common ground).

The elements are arrayed on a  $1\text{ cm} \times 1\text{ cm}$  chip in an  $8 \times 8$  pattern. There are 76 bond pads along two edges of the chip for



(a) SEM image tilted at a sixty degree angle of an element illustrating the corrugation, wire scheme, and tunnel concept for electrical connection to bottom electrode. Diaphragm is  $600\text{ }\mu\text{m}$ .



(b) SEM image of vent hole for static equilibrium of pressure.

Figure 4. SEM images of (a) diaphragm, corrugation around diaphragm, wire scheme, and tunnel concept, and (b) vent holes.

electrical connection. The direction of flow is bottom to top so the flow does not pass across the bond pads. The element center-to-center pitch in the direction of flow is  $1.2625\text{ mm}$  (which allows for multiple  $8 \times 8$  array to be placed end-to-end to determine low wavenumber information through the larger spatial scale), while the pitch across the flow is  $1.1125\text{ mm}$ . Packaging uses a pin grid array package to which the MEMS array is wirebonded. Laser cut spacers allow for the MEMS chip to be mounted flush with the package surface. Off chip electronics amplify the signal to a data acquisition enabled computer.

## MODELING AND DESIGN

A model for one individual microphone in the array is described. For each element in our design, a MATLAB® script was compiled to examine the response electrostatically as well as

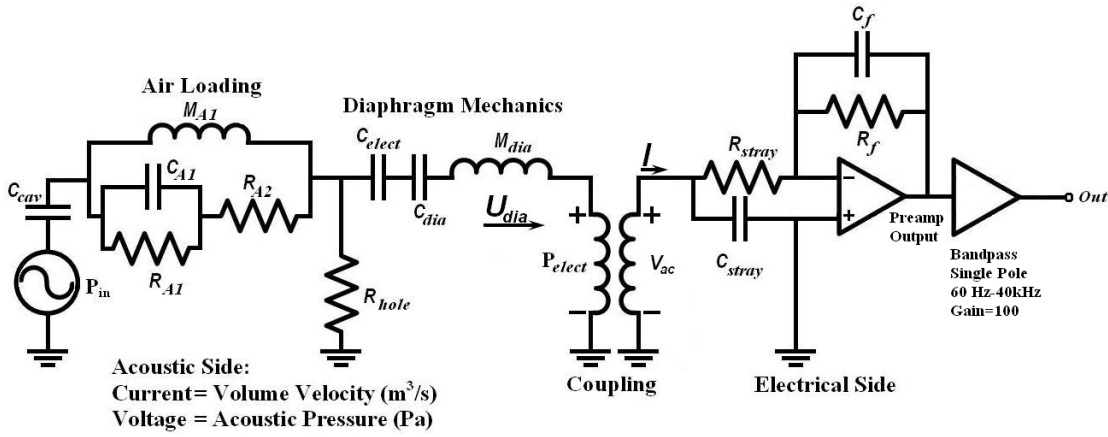


Figure 5. Coupled mechanical-electrical lumped element model.

to a unit pressure. The parameters of the script were computed following an acoustic lumped element circuit diagram shown in Figure 5. The compliance, resistance and mass of the microphone were accounted for in the circuit diagram and then implemented into the MATLAB® script. The compliances, resistances and mass loading of the microphones were computed using parameters from [9, 12, 13]. Using Beranek's solutions for environmental loading of the air we compute:

$$R_{A1} = \frac{0.1404\rho c}{a_{eff}^2} \quad (1)$$

$$R_{A2} = \frac{\rho c}{\pi a_{eff}^2} \quad (2)$$

$$M_{A1} = \frac{8\rho}{3\pi^2 a_{eff}^3} \quad (3)$$

$$C_{A1} = \frac{5.94a_{eff}^3}{\rho c^2} \quad (4)$$

$$C_{cav} = \frac{V_{gap}}{\rho c^2} \quad (5)$$

where  $\rho$  is the density of air,  $c$  is the speed of sound,  $a$  is the effective radius of the diaphragm (equal to 80% of the actual radius for a circular bending plate), and  $V_{gap}$  is the volume of the gap between the diaphragm and bottom electrode. From Martin *et al.* we compute resistance due to the holes in the diaphragm, the compliance of the diaphragm (for a clamped circular bending plate), and the effective mass of the diaphragm (for the first mode of the clamped circular bending plate) [9]:

$$R_{through} = \frac{72\mu t_{dia}}{n\pi a_{hole}^4} \quad (6)$$

$$C_{dia} = \frac{\pi a^6 (1 - \nu^2)}{16Et^3} \quad (7)$$

$$M_{dia} = \frac{9\rho t_{dia}}{5\pi a^2} \quad (8)$$

where  $\mu$  is the viscosity of air,  $t_{dia}$  is the thickness of the diaphragm,  $n$  is the number of holes in the diaphragm,  $a_{hole}$  is the radius of the holes in the diaphragm,  $\nu$  is Poisson's ratio, and  $E$  is the elastic modulus of the diaphragm. Using Škvor's formula, ( $S$ ), and calculating a correction factor, ( $C_f$ ) we can determine the resistance due to the squeeze film damping ( $R_{squeeze}$ ) [9, 14].

$$S = \frac{\pi a_{hole}^2}{C^2} \quad (9)$$

$$C_f = \frac{S}{2} - \frac{S^2}{8 - \frac{1}{4}\ln(S) - \frac{3}{8}} \quad (10)$$

$$R_{squeeze} = \frac{12\mu C_f}{n\pi t_{gap}^3} \quad (11)$$

The hole resistance in the circuit model is the series combination of the squeeze film damping,  $R_{squeeze}$  and the through-hole damping,  $R_{through}$ ,

$$R_{hole} = R_{squeeze} + R_{through} \quad (12)$$

where  $C_c$  is the center-to-center spacing of holes in the diaphragm. Using the above model for the microphone and using a coupling parameter,  $N$ , to relate the pressure to a voltage:

$$N = \frac{V_{bias}\epsilon}{t_{gap}^2} \quad (13)$$

where  $V_{bias}$  is the bias voltage applied to the bottom electrode,  $\epsilon$  is the permittivity of free space, and  $t_{gap}$  is the height of the air gap. This coupling parameter gives the acoustic pressure applied to the diaphragm for a given AC voltage on the electrical side, and, equivalently, the current into the electrical side in response to a given volume velocity of the diaphragm.

$$P_{elect} = N \cdot V_{ac} \quad (14)$$

$$I = N \cdot U_{dia} \quad (15)$$



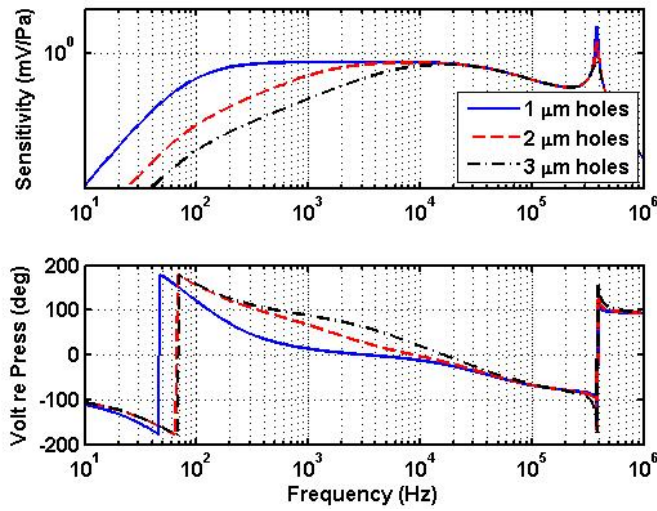


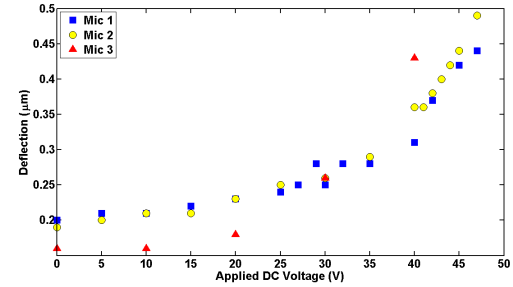
Figure 6. Predicted acoustic sensitivity for a single element with 9  $V_{bias}$ , showing the importance of the vent hole size. Hole sizes are shown with radii of 1, 2 and 3  $\mu\text{m}$ .

The sensitivity (voltage out per Pascal) can be computed as a function of frequency by incorporating the electronics which give the response curve its shape. The model for the receive electronics is a series combination of two single pole passive high pass filters with break frequencies of 60 Hz and 80 Hz, a charge amp with a gain of 100 mV/pC, and a voltage gain stage of 100 with a single pole low pass filter at 40 kHz. The final predicted pressure sensitivity results are shown in *Figure 6*. This is sensitivity at the bandpass output (40 dB above the preamp output in the pass-band). The predicted performance for the pressure sensor array is shown in *Table 1*. Varying the size of the vent holes has a major impact on the low frequency response as shown in *Figure 6*.

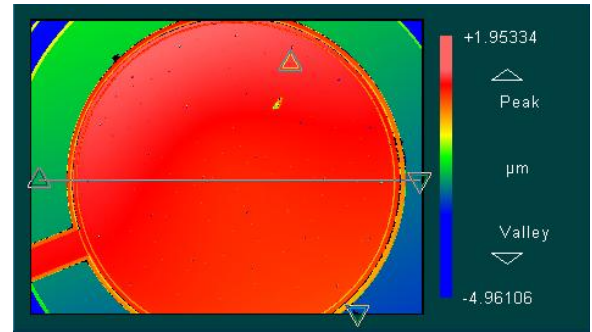
## RESULTS

The overall fabrication of the sensor was a success, however, there were a few design parameters that were not optimal. Examples of design constraints that were not met are the minimum feature size of 2  $\mu\text{m}$ , alignment of mask layers, a thinning of the silicon nitride layer, and etch times for releasing the oxide layer. *Figure 4* demonstrates some of the features of the microphone array after fabrication. As seen in *Figure 4b*, the largest problem to which has vast implications in the dynamics of the model is the alignment and increase in size of the vent holes in the diaphragm. The alignment issue was first a concern to whether the sacrificial oxide layer could be removed to release the membrane.

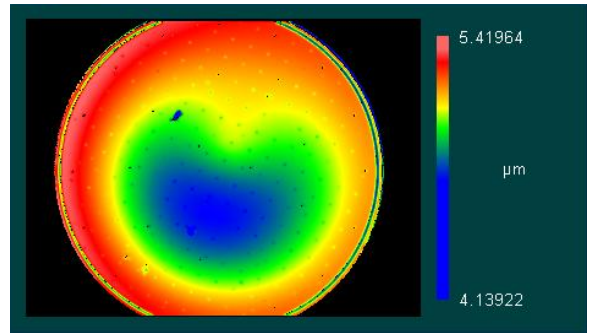
Several tests have been performed to validate that this is not the case. Capacitance tests before and after release indicate a reduction in capacitance which confirms the membrane has been



(a) Empirical data showing snapdown for three elements in the array. Theory predicts snapdown at 47 V.



(b) White light interferometer screenshot showing membrane with zero voltage applied



(c) White light interferometer screenshot showing membrane with 47 volts applied causing snapdown

Figure 7. White light interferometer data showing the surface profile of an element in the microphone array. Results show (a) plot of center point displacement as a function of voltage, (b) screenshot with 0 V applied, and (c) screenshot of snapdown at 47 V.

released. A non-contact white light interferometer measured the surface topology as a voltage was applied to the membrane to determine when snapdown would occur. The empirical results from this measurement followed closely to the theoretical results and is shown in *Figure 7a*. *Figure 7a* shows three different elements all showing a snapdown voltage close to 47 V precisely the voltage at which the membrane theoretically snaps down. These tests confirm that the membrane has been released.

Although the above results include variations of unexpected

Table 1. Predicted performance for pressure sensor array.

Performance Parameter	Value
Sensor Chip Size	1.01 cm x 1.01 cm
Number of Elements	64
Individual Sensor Diameter	0.6 mm
Sensor Center-to-Center Spacing (Pitch)	1.2625 mm
Sensor Bandwidth	480 kHz
Sensitivity of Individual Element	0.1 mV/Pa @ 1kHz 0.6 mV/Pa @ 10kHz
Sensitivity of Entire Array	6.4 mV/Pa @ 1kHz 38.4 mV/Pa @ 10kHz
Center Displacement of Element	0.005 nm/Pa @ 1kHz 0.029 nm/Pa @ 10kHz
Low Frequency Rolloff	515 Hz
Resistance of Trace	10-50 $\Omega$
Capacitance of Each Element	$\approx$ 50 pF $\approx$ 48.4 pF stray $\approx$ 1.3 pF active
Individual Element Dynamic Range*	85-150 dB SPL 97-150 dB SPL
In-Phase Array Dynamic Range*	57-150 dB SPL 61-150 dB SPL

\*Note: dynamic ranges are due to two different noise models

results due to the fabrication process, the fabrication process is considered a success due to the fact that there was no stiction of the membrane in normal circumstances, no buckling of the membrane, and static stiffness reports due to displacement measurements corresponded to theoretical predictions.

Laser Doppler velocimetry (LDV) is used to measure the centerpoint vibration of the diaphragm in response to an applied AC voltage plus DC bias. The results of the measurement show a strong, high Q resonance at 480 kHz. The frequency of the resonance is strongly influenced not only by the bending stiffness of the diaphragm, but also by the acoustic stiffness coming from the backing cavity and the environmental acoustic impedance. *Figure 8* shows a comparison between the measured electrostatic frequency response and the model predictions. The model does a good job of predicting the primary resonance frequency and

the shape of the low frequency magnitude curve. The differences between the two types of encoding is due to a filter on the LDV system does not allow the displacement encoder to measure below 100 kHz and does not allow the velocity decoder to measure above 100 kHz.

Acoustic calibration is performed in a plane wave tube with the array flush mounted into a plate at the end of the tube. A 1/4" B&K pressure microphone is flush mounted in close proximity to the array. We cannot calibrate reliably above 3 kHz with the current setup due to the onset of non-plane crossmodes in the tube. The sensitivity measurements are shown in *Figures 9* and *10*. Acoustic calibration shows sensitivity that changes linearly with applied bias, as seen in *Figure 9*. The sensitivity at the band-pass output with 9 volts bias is on the order of 2 mV/Pa at 1 kHz, for 16 elements operating in parallel (thus, approximately 0.13

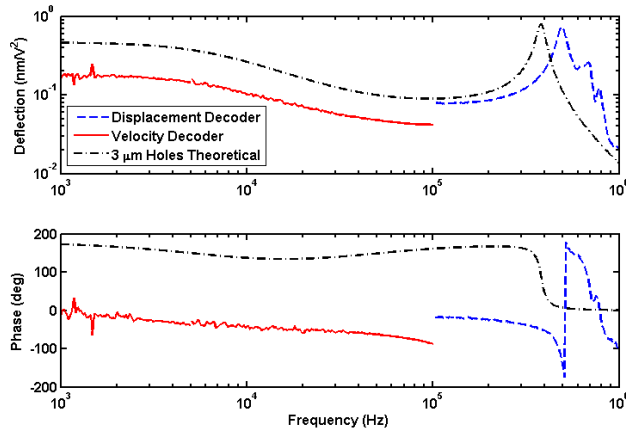


Figure 8. Laser Doppler velocimetry (LDV) measurements as a result of an electrostatic excitation to the microphone.

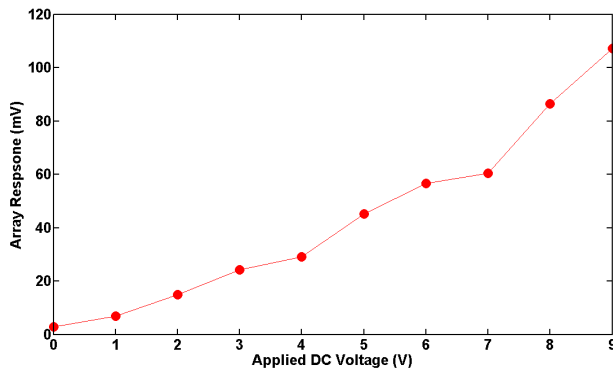


Figure 9. Plot of the response of 16 elements in the microphone array to a constant drive signal at 1 kHz versus the change in bias applied. Testing is in a Faraday cage and a plane wave tube attached to a six inch horn device.

mV/Pa for an individual element). These results show the sensitivity rising as a function of frequency, in reasonable agreement with the model for 3 micron diameter holes. Initial results comparing matching across the array were conducted. Comparing the sensitivity of 16 elements in the array at 1 kHz, we see a standard deviation of 0.025 mV/Pa (20 %). Further characterization of array repeatability and sensitivity is ongoing.

## CONCLUSION

A surface micromachined, front-vented, 64 channel (8×8), capacitively sensed pressure sensor array for aeroacoustic analysis of the turbulent boundary layer has been designed and characterized. Modeling shows an understanding of the dynamics of the sensor and anticipated results of future designs can ben-

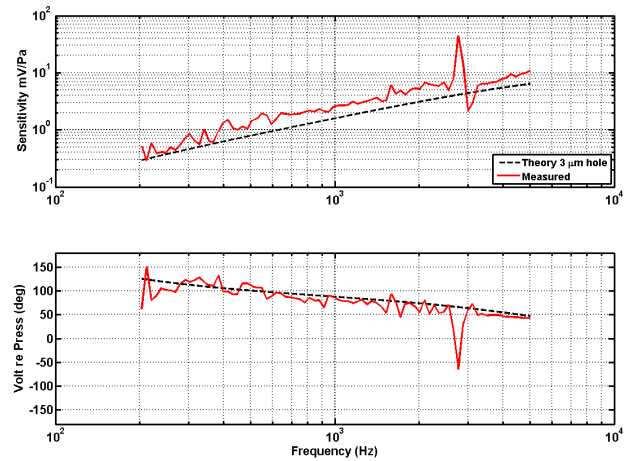


Figure 10. Plot of 16 elements (in parallel) of MEMS device versus a type 3939 B&K microphone. Testing is in a Faraday cage and a plane wave tube attached to a six inch horn device. Plot shows similar trend versus theoretical values.

efit as a result of this working knowledge. The dynamics of this microphone incorporate a lumped element model that accurately predicts the response of the microphone array using various MATLAB® scripts. Theory predicts single element sensitivity of 0.591 mV/Pa and displacement of 0.029 nm at the gain stage output in the 400-40,000 Hz band and a strong first resonance at 480 kHz.

Layout of the MEMS sensor array shows promise due to size and spatial patterning. This is the first known fine pitched MEMS pressure sensor array on a single chip with characteristic length and size scales needed for turbulent boundary layer measurements. The array is fabricated with a center-to-center pitch of 1.2625 mm allowing for low wavenumbers to be resolved by spacing multiple chips end-to-end. The fine pitch will allow for high resolution data on the frequency-wavenumber spectra of the TBL experienced by an aircraft in flight.

The pressure sensor array was fabricated using the MEMSCAP PolyMUMPs® process, a three layer polysilicon surface micromachining foundry process. A successful, fully surface micromachined front-vented, 64 element, capacitively sensing pressure sensor has demonstrated acoustic sensitivity due to the fabrication techniques derived from this process. Although problems originated from fabrication flaws, knowledge of and subsequent runs in the PolyMUMPs process can account for these variations in fabrication processes. Limitations of the PolyMUMPs process should be analyzed to determine if a customized process is needed for future designs.

Preliminary acoustic calibrations shows single element acoustic sensitivity (as a function of frequency) increasing from 0.01 mV/Pa at 200 Hz to 0.16 mV/Pa at 2 kHz. A laser Doppler



velocimetry (LDV) system has been used to map the spatial motion of the elements in response to electrostatic excitation. A strong resonance appears at 480 kHz from electrostatic excitation, which is in good agreement with mathematical models. Static stiffness measured electrostatically using an interferometer is  $0.1 \text{ nm/V}^2$ , similar to the expected stiffness.

The next steps for this work are to attempt Parylene coating of the current microphone array in order to decrease the size of the vent holes and extend the low frequency bandwidth. This will have the added benefit of protecting the sensor from the environment. The sensor also needs to be potted, and a high frequency calibration method (above 2 kHz) established. Once this is accomplished, the next step would be to test the array in a wind tunnel. Issues such as sensitivity to temperature, static pressure changes, and moisture will also have to be characterized. Design of thermal stress relief and system level integration of temperature sensors will need to be characterized in a laboratory setting to determine the temperature sensitivity. Similarly for the static pressure changes, the front-venting static pressure equalization will need to be characterized in a laboratory setting to determine the static pressure sensitivity. Sensitivity to moisture will be minimized by deposition of a moisture resistant coating such as Parylene over the entire packaged array. Packaging reliability will be a key factor in our future efforts to produce a flight-worthy array.

## REFERENCES

- [1] H. Tennekes and J. L. Lumley. *A First Course in Turbulence*. The MIT Press, 1972.
- [2] J. F. Wilby and F. L. Gloyna. Vibration measurements of an airplane fuselage structure ii. jet noise excitation. *Journal of Sound and Vibration*, 23(4):467–486, August 1972.
- [3] W. R. Graham. A comparison of models for the wavenumber-frequency spectrum of turbulent boundary layer pressures. *Journal of Sound and Vibration*, 206(4):541–565, October 1997.
- [4] B. M. Abraham and W. L. Keith. Direct measurements of turbulent boundary layer wall pressure wavenumber-frequency spectra. *Journal of Fluids Engineering*, 120:29–39, March 1998.
- [5] G. M. Corcos. Resolution of pressure in turbulence. *The Journal of the Acoustical Society of America*, 35(2):192–199, February 1962.
- [6] G. M. Sessler. Acoustic sensors. *Sensors and Actuators A: Physical*, 26(1-3):323–330, March 1991.
- [7] P. R. Scheeper, A. G. H. van der Donk, W. Olthuis, and P. Bergveld. A review of silicon microphones. *Sensors and Actuators A: Physical*, 44(1):1–11, July 1994.
- [8] Lennart Löfdahl and Mohamed Gad-el Hak. Mems applications in turbulence and flow control. *Progress in Aerospace Sciences*, 35:101–203, 1999.
- [9] David T. Martin, Jian Liu, Karthik Kadirvel, Robert M. Fox, Mark Sheplak, and Toshikazu Nishida. A micro-machined dual-backplate capacitive microphone for aeroacoustic measurements. *Journal of Microelectromechanical Systems*, 16(6):1289–1302, 2007.
- [10] Robert W. Johnstone and M. Parameswaran. Mumps design handbook: Unofficial supplement. [Internet], Available at: <http://www.sfu.ca/immr/>, 2002.
- [11] Jing Chen, Litian Liu, Zhijian Li, Zhimin Tan, Yang Xu, and Jun Ma. Single-chip condenser miniature microphone with high sensitive circular corrugated diaphragm. *Proceedings of the IEEE Micro Electro Mechanical Systems (MEMS)*, pages 284–287, 2002.
- [12] Leo L. Beranek. *Acoustics*. Acoustical Society of America, 1996.
- [13] Lawrence E. Kinsler, Austin R. Frey, Alan B. Coppens, and James V. Sanders. *Fundamentals of Acoustics: Fourth Edition*. John Wiley & Sons, 2000.
- [14] D. Homencovski and R.N. Miles. Viscous damping of perforated planar micromechanical structures. *Sensors and Actuators A: Physical*, 119(2):544–552, April 2005.